NUCL SCI TECH (2019) 30:64
https://doi.org/10.1007/s41365-019-0580-8

Study of spatial resolution of the associated alpha particle imaging–time-of-flight method

Meng Huang[1] · Jian-Yu Zhu[1] · Jun Wu[1]

Received: 3 August 2018 / Revised: 14 October 2018 / Accepted: 20 October 2018 / Published online: 18 March 2019

Abstract Associated alpha particle imaging based on the time-of-flight (API-TOF) technique is an advanced neutron analysis method, which is capable of discriminating material nuclides and three-dimensional imaging of the spatial distribution of material nuclei. In this paper, the spatial resolution of API-TOF and its effects are studied using mathematical analysis and Monte Carlo numerical simulation. The results can provide guidance and assist in designing of API-TOF detection devices. First, a mathematical analysis of the imaging principles of the API-TOF was carried out, and the calculation formulas of the spatial resolution of API-TOF were deduced. Next, the relationship between the device layout and the spatial resolution of the API-TOF detection device was studied. The concept of a typical API-TOF detection device with an optimized structure was proposed. Then, the spatial distribution of the spatial resolution of the typical API-TOF detection device was analyzed, and the effects of the time resolution and the neutron emission angle resolution on the spatial resolution were studied. The results show that spatial resolutions better than 1 cm can be achieved by improving the time resolution and the neutron emission angle resolution to appropriate levels. Finally, a Monte Carlo numerical simulation program was developed for the study of the API-TOF and was used to calculate the spatial resolutions of the API-TOF. The comparison of the results shows that the spatial resolutions calculated based on the Monte Carlo numerical simulation are in good agreement with those calculated based on the mathematical analysis. This verifies the mathematical analysis and the evaluation of the effects of the spatial resolution of the API-TOF in this study.

Keywords API-TOF · Spatial resolution · Mathematical analysis · Monte Carlo numerical simulation

1 Introduction

Associated alpha particle imaging based on the time-of-flight technique (API-TOF) is an advanced neutron analysis method. It is capable of discriminating material nuclides and three-dimensional (3D) imaging of the spatial distribution of material nuclei. The two fundamental steps of API-TOF are as follows: (1) The inspected object is irradiated by 14.1-MeV neutrons from a deuterium–tritium (DT) neutron source, and the neutrons scatter inelastically on or enter into nuclear reactions with the nuclei of the inspected object, producing characteristic γ-rays. The types of the nuclei reacting with the incident neutrons can be determined by measuring the energies of the γ-rays. (2) Alpha particles are produced by DT reactions ($^{2}H + {}^{3}H \rightarrow {}^{4}He + n$), and an alpha particle detector is used to detect the emission direction and emission time of the recoiled alpha particle produced by the DT neutron source. By combining these with the time of the γ-ray arriving at the γ-ray detector, the emission direction of the 14.1-MeV neutrons and the total flight time of the neutron and the γ-ray can be obtained, and the position of the nucleus reacting with the 14.1-MeV neutrons can be reconstructed

✉ Jian-Yu Zhu
zhujyu@126.com

Meng Huang
hm.max@126.com

1 Center for Strategic Studies, China Academy of Engineering Physics, Beijing 100088, China

[1, 2]. Compared with other neutron analysis techniques, such as thermal neutron analysis, fast neutron analysis, and pulsed fast/thermal neutron analysis, the API-TOF has two advantages: (1) It records the 14.1-MeV neutrons by detecting alpha particles, which can suppress the interference from the background and improve the signal-to-noise ratio and (2) it capable of the 3D imaging of spatial distribution of material nuclei and can analyze the geometric shapes and material distributions of the inspected objects in depth.

In recent years, the related research of API-TOF has been carried out worldwide, and it was applied in the fields of explosive detection, customs inspection, arms control verification, and so on. Since the 1990s, initial studies have been performed in the USA, resulting in a performance improvement in the DT neutron tubes and γ-ray detectors used in API-TOF detection devices [1–6]. Since the beginning of the twenty-first century, research related to API-TOF has been carried out in Russia, and a prototype device capable of distinguishing explosives and non-explosive materials has been developed [7–9]. Since 2005, a number of European countries, including France, Italy, Poland, and Croatia, have funded EURITRACK Project, and a tagged neutron inspection system (TNIS) based on API-TOF has been developed, which is to be used to detect smuggled goods at customs, such as drugs and explosives. In 2007, a prototype of the TNIS was installed and operated in the port of Rijeka, Croatia, which could discriminate explosives from common materials by analyzing the measured γ-ray spectra [10–15]. In 2014, a set of explosive detection devices based on API-TOF was developed in China, which was already capable of distinguishing explosives and non-explosive materials [16, 17]. In general, the research on API-TOF has mainly focused on the identification of materials, and the research on the image reconstruction ability of API-TOF is still in its initial stage. The research on the spatial resolution of API-TOF and on its effects is especially limited, which is a problem that needs to be solved in the design and performance assessment of API-TOF detection devices.

In this paper, the spatial resolution of API-TOF and its effects are studied by mathematical analysis and Monte Carlo numerical simulation. The results of this research are expected to provide guidance and assist the design of API-TOF detection devices. This paper is divided into six sections: Sect. 1 is an introduction, Sect. 2 presents a mathematical analysis of the imaging principles of API-TOF and deduces the calculation formulas for the spatial resolution of the API-TOF, and in Sect. 3 the relationship between the device layout and the spatial resolution of the API-TOF detection device is discussed and a concept of a typical API-TOF detection device with an optimized structure is proposed. Section 4 provides an analysis of the spatial distribution of the spatial resolution of a typical API-TOF detection device and studies the effects of the time resolution and the neutron emission angle resolution on the spatial resolution. In Sect. 5, a study on the spatial resolution of the API-TOF by Monte Carlo numerical simulation is presented, and in Sect. 6 the conclusion of this study is drawn.

2 Mathematical analysis of the spatial resolution of the API-TOF

As mentioned above, the API-TOF uses the direction of the neutron emission and the total flight time of the 14.1-MeV neutrons and γ-rays, which are given by the alpha particle detector and γ-ray detector of the API-TOF detection device, to reconstruct the spatial position of the nucleus reacting with the 14.1-MeV neutron, thus realizing 3D imaging of the spatial distribution of material nuclei. To analyze the spatial resolution of the API-TOF in depth, a simplified physical model of the API-TOF detection device was constructed, as shown in Fig. 1. In this model, the neutron source is represented by a point source and located at position (x_1, y_1, z_1). A 14.1-MeV neutron emitted from the neutron source reacts with nucleus A of the inspected object at position (x, y, z), and a characteristic γ-ray is produced. The characteristic γ-ray enters the γ-ray detector and deposits energy at position (x_2, y_2, z_2), and then, a signal is produced. Based on this model, the spatial position of nucleus A reacting with the 14.1-MeV neutron can be calculated from the direction of neutron emission and the total flight time of the neutron and the γ-ray. The detailed formula can be obtained as follows.

First, vector (θ, φ) is used to represent the neutron emission direction: θ is the angle between the neutron emission direction and the positive direction of the z-axis, and φ is the angle between the projection of the neutron emission direction on the x–y plane and the positive direction of the x-axis. To simplify the deduction of the

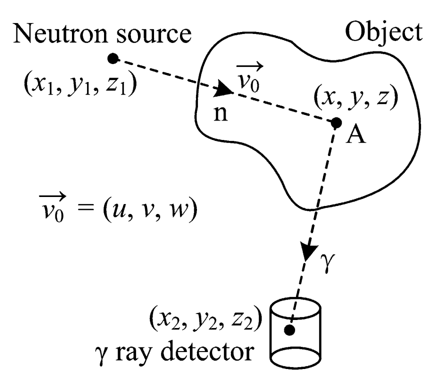

Fig. 1 Simplified physical model of the API-TOF detection device

formula, the space vector (u, v, w) is introduced to represent the direction of neutron emission, which has the following relationship with θ and φ:

$$\begin{cases} u = \sin\theta \cdot \cos\varphi \\ v = \sin\theta \cdot \sin\varphi \\ w = \cos\theta \end{cases}. \tag{1}$$

Furthermore, the relationship between the neutron emission direction (u, v, w), the neutron source location (x_1, y_1, z_1), and the spatial position of the nucleus A (x, y, z) is given by

$$\frac{x - x_1}{u} = \frac{y - y_1}{v} = \frac{z - z_1}{w}. \tag{2}$$

Then, the relationship between the total flight time of the neutron and γ-ray (t), the neutron source location (x_1, y_1, z_1), the spatial position of nucleus A (x, y, z), and the reaction position of the γ-ray in the detector (x_2, y_2, z_2) can be written as

$$\begin{aligned} &\frac{\sqrt{(x-x_1)^2 + (y-y_1)^2 + (z-z_1)^2}}{v_0} \\ &\quad + \frac{\sqrt{(x-x_2)^2 + (y-y_2)^2 + (z-z_2)^2}}{c} \\ &\quad = t, \end{aligned} \tag{3}$$

where v_0 is the speed of 14.1-MeV neutron and c is the speed of light.

Finally, by combining Eqs. (2) and (3), the spatial position (x, y, z) of nucleus A can be expressed as

$$\begin{cases} x = uk + x_1 \\ y = vk + y_1 \\ z = wk + z_1 \end{cases}, \tag{4}$$

where k is given by

$$\begin{aligned} k &= \frac{-Q + \sqrt{Q^2 - 4PR}}{2P} \\ P &= 1 - \frac{c^2}{v_0^2} \\ Q &= \frac{2c^2 t}{v_0} + 2u(x_1 - x_2) + 2v(y_1 - y_2) + 2w(z_1 - z_2) \\ R &= -c^2 t^2 + (x_1 - x_2)^2 + (y_1 - y_2)^2 + (z_1 - z_2)^2. \end{aligned} \tag{5}$$

In the 3D imaging of the spatial distribution of material nuclei based on API-TOF, θ, φ, and t are given by three independent measurements. Due to the uncertainties of these three measurements, the reconstructed positions of the material nuclei also have uncertainties. The standard deviations (also uncertainties) of the reconstructed x-, y-, and z-coordinates of the material nucleus are defined as the spatial resolutions of the API-TOF detection device and are denoted by δx, δy, and δz, respectively. The standard deviations of the measurements of θ and φ are defined as the neutron emission angle resolutions and are denoted by $\delta\theta$ and $\delta\varphi$, respectively. The standard deviation of the measurements of t is defined as the time resolution and is denoted by δt. $\delta\theta$ and $\delta\varphi$ are mainly determined by the measurement accuracy of the alpha particle detector for the emission directions of the recoiled alpha particles, while δt is mainly determined by the timing accuracies of the alpha particle detector and the γ-ray detector.

It should be noted that in this paper, the measurements of θ, φ, and t are their estimates as well. Based on the Cramér–Rao lower bound [18], it can be proved that the measurements of θ, φ, and t are the best unbiased estimates of θ, φ, and t. For example, the probability distribution of θ approximately follows a Gaussian distribution

$$p(\theta_\mathrm{m}; \theta) = \frac{1}{\sqrt{2\pi\sigma^2}} \mathrm{e}^{-\frac{1}{2\sigma^2}(\theta_\mathrm{m} - \theta)^2}, \tag{6}$$

where θ_m is the measurement of θ and σ is the uncertainty of θ_m. According to the Cramér–Rao lower bound, the deviation of the unbiased estimate ($\hat{\theta}$) of θ has a lower bound

$$\mathrm{var}(\hat{\theta}) \geq \frac{1}{-E\left[\frac{\partial^2 \ln p(\theta_\mathrm{m};\theta)}{\partial\theta^2}\right]} = \sigma^2, \tag{7}$$

where E is an operator calculating the expected value. If the measurement θ_m is chosen as an estimate of θ, the deviation of the estimate becomes

$$\mathrm{var}(\hat{\theta}) = \mathrm{var}(\theta_\mathrm{m}) = \sigma^2. \tag{8}$$

Therefore, the measurement of θ is the best unbiased estimate of θ. This result is also applicable to φ and t. In the rest of this paper, the measurements and the estimates of θ, φ, and t are not distinguished and they are all expressed as θ, φ and t.

Furthermore, based on the reconstruction formula of the spatial positions of the nuclei obtained above, the relationship between the spatial resolution of the API-TOF (δx, δy, δz) and $\delta\theta$, $\delta\varphi$, δt can be deduced as follows. First, based on the error propagation formula it is known that

$$\begin{cases} \delta x = \sqrt{\left(\frac{\partial x}{\partial\theta}\right)^2 \delta\theta^2 + \left(\frac{\partial x}{\partial\varphi}\right)^2 \delta\varphi^2 + \left(\frac{\partial x}{\partial t}\right)^2 \delta t^2} \\ \delta y = \sqrt{\left(\frac{\partial y}{\partial\theta}\right)^2 \delta\theta^2 + \left(\frac{\partial y}{\partial\varphi}\right)^2 \delta\varphi^2 + \left(\frac{\partial y}{\partial t}\right)^2 \delta t^2} \\ \delta z = \sqrt{\left(\frac{\partial z}{\partial\theta}\right)^2 \delta\theta^2 + \left(\frac{\partial z}{\partial\varphi}\right)^2 \delta\varphi^2 + \left(\frac{\partial z}{\partial t}\right)^2 \delta t^2} \end{cases}, \tag{9}$$

where

$$\frac{\partial x}{\partial \theta} = \frac{\partial u}{\partial \theta}\cdot k + u\cdot\frac{\partial k}{\partial \theta}, \frac{\partial x}{\partial \varphi} = \frac{\partial u}{\partial \varphi}\cdot k + u\cdot\frac{\partial k}{\partial \varphi}, \frac{\partial x}{\partial t} = u\cdot\frac{\partial k}{\partial t}$$
$$\frac{\partial y}{\partial \theta} = \frac{\partial v}{\partial \theta}\cdot k + v\cdot\frac{\partial k}{\partial \theta}, \frac{\partial y}{\partial \varphi} = \frac{\partial v}{\partial \varphi}\cdot k + v\cdot\frac{\partial k}{\partial \varphi}, \frac{\partial y}{\partial t} = v\cdot\frac{\partial k}{\partial t}$$
$$\frac{\partial z}{\partial \theta} = \frac{\partial w}{\partial \theta}\cdot k + w\cdot\frac{\partial k}{\partial \theta}, \frac{\partial z}{\partial \varphi} = \frac{\partial w}{\partial \varphi}\cdot k + w\cdot\frac{\partial k}{\partial \varphi}, \frac{\partial z}{\partial t} = w\cdot\frac{\partial k}{\partial t}. \tag{10}$$

Then, based on Eq. (1), the expressions for $\frac{\partial u}{\partial \theta}$, $\frac{\partial u}{\partial \varphi}$, $\frac{\partial v}{\partial \theta}$, $\frac{\partial v}{\partial \varphi}$, $\frac{\partial w}{\partial \theta}$, and $\frac{\partial w}{\partial \varphi}$ can be obtained as

$$\frac{\partial u}{\partial \theta} = \cos\theta\cdot\cos\varphi,\ \frac{\partial u}{\partial \varphi} = -\sin\theta\cdot\sin\varphi$$
$$\frac{\partial v}{\partial \theta} = \cos\theta\cdot\sin\varphi,\ \frac{\partial v}{\partial \varphi} = \sin\theta\cdot\cos\varphi \tag{11}$$
$$\frac{\partial w}{\partial \theta} = -\sin\theta,\ \frac{\partial w}{\partial \varphi} = 0.$$

Next, based on Eq. (5), the expressions of $\frac{\partial k}{\partial \theta}$, $\frac{\partial k}{\partial \varphi}$, and $\frac{\partial k}{\partial t}$ can be written as

$$\frac{\partial k}{\partial \theta} = -\frac{\partial Q}{\partial \theta}\cdot\frac{k}{2kP+Q}$$
$$\frac{\partial k}{\partial \varphi} = -\frac{\partial Q}{\partial \varphi}\cdot\frac{k}{2kP+Q} \tag{12}$$
$$\frac{\partial k}{\partial t} = \frac{2tc^2}{2kP+Q} - \frac{\partial Q}{\partial t}\cdot\frac{k}{2kP+Q},$$

where

$$\frac{\partial Q}{\partial \theta} = 2(x_1-x_2)\frac{\partial u}{\partial \theta} + 2(y_1-y_2)\frac{\partial v}{\partial \theta} + 2(z_1-z_2)\frac{\partial w}{\partial \theta}$$
$$\frac{\partial Q}{\partial \varphi} = 2(x_1-x_2)\frac{\partial u}{\partial \varphi} + 2(y_1-y_2)\frac{\partial v}{\partial \varphi}$$
$$\frac{\partial Q}{\partial t} = \frac{2c^2}{v_0}. \tag{13}$$

Finally, the mathematical analysis of the spatial resolution (δx, δy, δz) of API-TOF can be completed by substituting Eqs. (10), (11), (12), and (13) into Eq. (9).

It should be noted that, in the mathematical model of the API-TOF detection device, the neutron source is defined as a point in the simplified model, as the target size of the DT neutron source (several millimeters) is much smaller than that of the detection area (tens of cm). The target size of the DT neutron source contributes to the spatial resolution of the API-TOF detection device and affects the neutron emission angle resolution. In addition, the reaction position of the incident γ-ray in the detector is assumed to be a point. As the photoelectron produced by the γ-ray in the detector produces a track, it is possible the arriving time of the γ-ray recorded by the detector does not accurately correspond to the reaction position of the γ ray recorded by the detector. The deviation can also affects the spatial resolution of the API-TOF detection device, and its effect contributes to the time resolution of the API-TOF detection device. Therefore, the effects of the target size of the DT neutron source and the photoelectron track on the spatial resolution of the API-TOF detection device are included in the neutron emission angle resolution and the time resolution, respectively; thus, the point models of the neutron source and the reaction position of the γ-ray in the detector are reasonable.

3 Relationship between device layout and spatial resolution of the API-TOF detection device

To determine a suitable layout for the API-TOF detection device, the relationship between the device layout, including the arrangement of the neutron source and the γ-ray detector, and the spatial resolution of the API-TOF detection device was studied based on the formulas in Sect. 2. In the simplified model, the neutron source was set as a point source, and its effective beam angle, where the directions of the emitting neutrons can be given by the alpha particle detector, was 180°, corresponding to a solid angle of 2π. The γ-ray detector was defined as a point in the simplified model, and it was assumed that certain γ-rays could just reach the point; the detection area was set as a sphere with the center at the origin and a radius of 50 cm. The size of the γ-ray detector affects the spatial resolution of the API-TOF detection device. However, as the size of the γ-ray detector is typically much smaller than the size of the detection area, the effect is negligible in the discussion of this section. The time resolution (δt) of the API-TOF detection device was 100 ps, and the neutron emission angle resolution was 1°; thus, $\delta\theta$ and $\delta\varphi$ were both 1°. In this section, the effects of the distance between the neutron source and the center of the detection area (L_1), the distance between the γ-ray detector and the center of the detection area (L_2), and the angle between the neutron source and the γ-ray detector relative to the center of the detection area (α) on the spatial resolution of the API-TOF detection device are discussed, and an optimization scheme for the structure of the API-TOF detection device is presented. It should be noted that following the adjustment of the device layout, the API-TOF detection device is fixed when the measurement begins, to be able to accurately reconstruct the positions of the material nuclei. As a result, the effects due to the movements of the neutron source and the γ-ray detector do not arise.

Figure 2a shows the effect of the distance between the neutron source and the center of the detection area (L_1) on the spatial resolution at the origin; the neutron source moves on the positive semi-axis of the x-axis, and the γ-ray

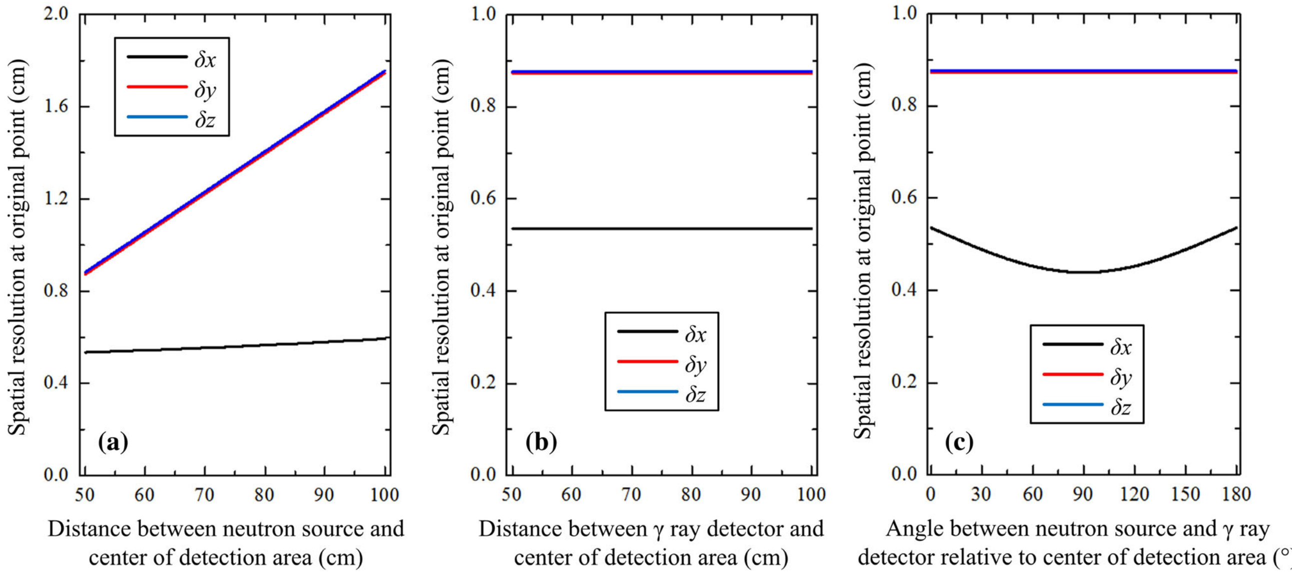

Fig. 2 (Color online) Study for the optimization of the structure of the API-TOF detection device (the red and blue lines coincide in all three figures)

detector is fixed at the position (0, 0, −50 cm). As shown in Fig. 2a, δx, δy, and δz at the origin increase with the increase in L_1, and the rates of the increase in δy and δz are significantly higher than that of δx. Therefore, to achieve better spatial resolutions in the detection area, the neutron source needs to be as close as possible to the detection area. Figure 2b shows the effect of the distance between the γ-ray detector and the center of the detection area (L_2) on the spatial resolution at the origin; the neutron source is fixed at the position (50 cm, 0, 0), and the γ-ray detector moves on the negative semi-axis of the z-axis. It can be seen that δx, δy, and δz at the origin have no relationship with L_2. However, in practical applications, the γ-ray detector needs to be located as close as possible to the detection area to improve its effective count rate. Figure 2c shows the effect of the angle between the neutron source and the γ-ray detector relative to the center of the detection area (α) on the spatial resolution at the origin; the neutron source is fixed at the position (50 cm, 0, 0), and the γ-ray detector moves on the x–z plane at a distance of 50 cm from the origin. It can be seen that δy and δz at the origin are independent of α, and δx at the origin reaches the minimum when α is 90°. Therefore, to achieve better spatial resolutions near the center of the detection area, α needs to be set as 90°.

The above analysis indicates that to achieve better image reconstruction results in the detection area in a short time, the neutron source and the γ-ray detector need to be as close as possible to the detection area, provided that the effective beam angle can cover the detection area, and the angle between the neutron source and the γ-ray detector relative to the center of the detection area needs to be set as 90°. In this paper, an API-TOF detection device that meets the requirements above is termed “typical API-TOF detection device.” Currently, most of the API-TOF prototypes developed worldwide meet the overall requirements of the typical API-TOF detection devices.

4 Spatial resolution analysis of the typical API-TOF detection device

In this section, the spatial distribution and the effects of the spatial resolution of the typical API-TOF detection device are studied, aiming to understand the imaging results of API-TOF in depth. In this section, it is assumed that the neutron source is a point source located at the position (50 cm, 0, 0) with an effective beam angle of 180°. The γ-ray detector is defined as a point in the simplified model located at the position (0, 0, − 50 cm); the detection area is set as a sphere with the center at the origin and a radius of 50 cm (see Fig. 3). The time resolution (δt) of the typical API-TOF detection device is 100 ps, and the neutron emission angle resolution is 1°. Thus, $\delta\theta$ and $\delta\varphi$ are both 1°.

Using the formulas in Sect. 2, the spatial distribution of the spatial resolutions (δx, δy, δz) of the typical API-TOF detection device can be calculated based on the model shown in Fig. 4. As shown in Fig. 4, δx decreases at a certain point on the x-axis with the increase in the distance between the point and the neutron source, while the trend of variation in δy and δz is exactly the opposite. At the same time, the rates of variation in δy and δz on the x-axis are much higher than that of δx; thus, the overall results of

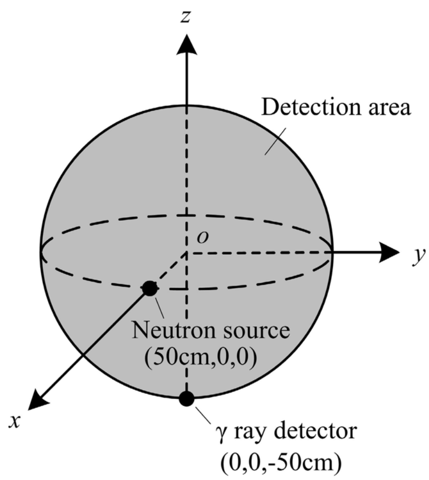

Fig. 3 Model of the typical API-TOF detection device

the image reconstruction in the detection area close to the neutron source are better. At a certain point, δx, δy, and δz increase on the y-axis with the increase in the distance between the point and the neutron source, while the variation rates of δx and δz on the y-axis are much higher than that of δy, and the variation rates of the former two increase with the increase in the distance between the point and the origin. Therefore, it can be further concluded that the image reconstruction results in the area close to the x–z plane are much better than those in the area far from the x–z plane. At a certain point, δx and δz decrease on the z-axis first and then increase with the increase in the distance between the point and the γ-ray detector, and δx shows a stronger variation, while δy remains unchanged on the z-axis. In addition, it can be found that the overall results of the image reconstruction in the area close to the x–y plane are better than those in the area far from the x–y plane using the model parameters above.

Next, the spatial resolution of the typical API-TOF detection device is analyzed based on the model above in the cases of different time resolutions (δt) and neutron emission angle resolutions ($\delta\theta$, $\delta\varphi$). The parameters of the model used here are the same as those of the model above except for the time resolution and the neutron emission angle resolution. Figure 5 shows the relationship between δx, δy, and δz at the origin and at $\delta\theta$, $\delta\varphi$, and δt. It can be seen that δx increases with the increase in $\delta\theta$, $\delta\varphi$, and δt, and the effect of $\delta\theta$ and $\delta\varphi$ on δx becomes small when δt is greater than 500 ps, provided that $\delta\theta$ and $\delta\varphi$ are smaller than 5°. Therefore, a high resolution of the neutron emission angle is unnecessary for the typical API-TOF detection device with low time resolution ($\delta t > 500$ ps). In addition, δy and δz increase with the increase in $\delta\theta$ and $\delta\varphi$, but they are independent of δt; thus, δt mainly affects δx in the vicinity of the origin. As shown in Fig. 5, that in order to achieve spatial resolutions better than 1 cm under the current model parameters, that is, δx, δy, and δz are all less than 1 cm, the neutron emission angle resolution ($\delta\theta$, $\delta\varphi$) of the typical API-TOF detection device needs to be at least 1° and the time resolution (δt) needs to be better than 200 ps.

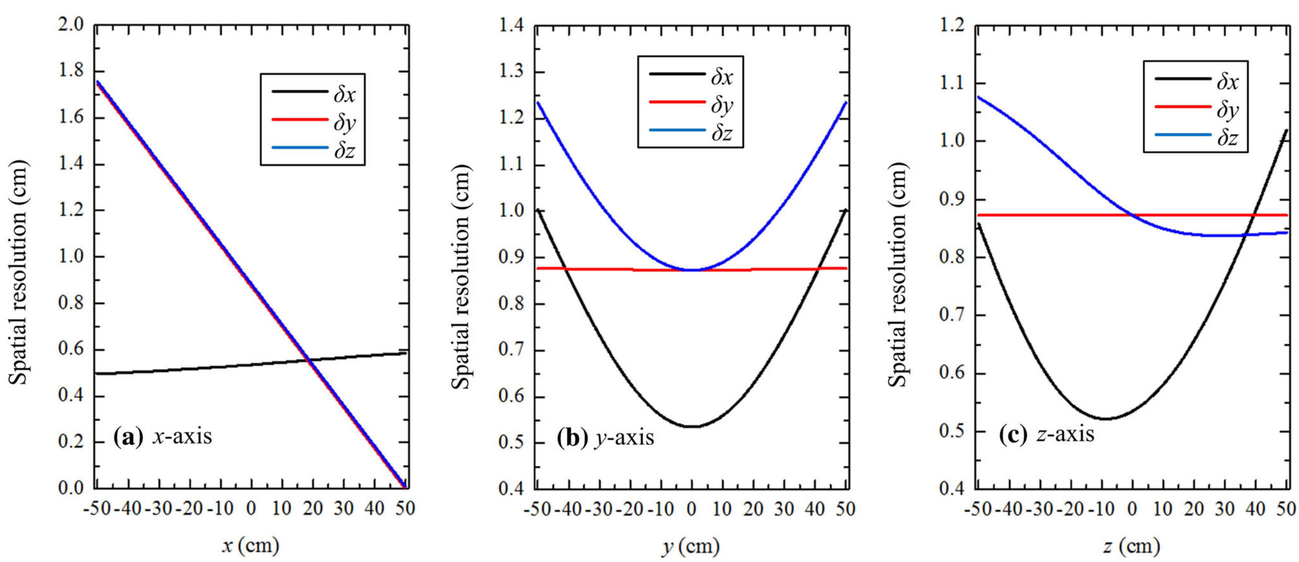

Fig. 4 (Color online) Trends of variation in spatial resolutions of the typical API-TOF detection device on the x-, y-, and z-axes [in (**a**), the red and blue lines coincide]

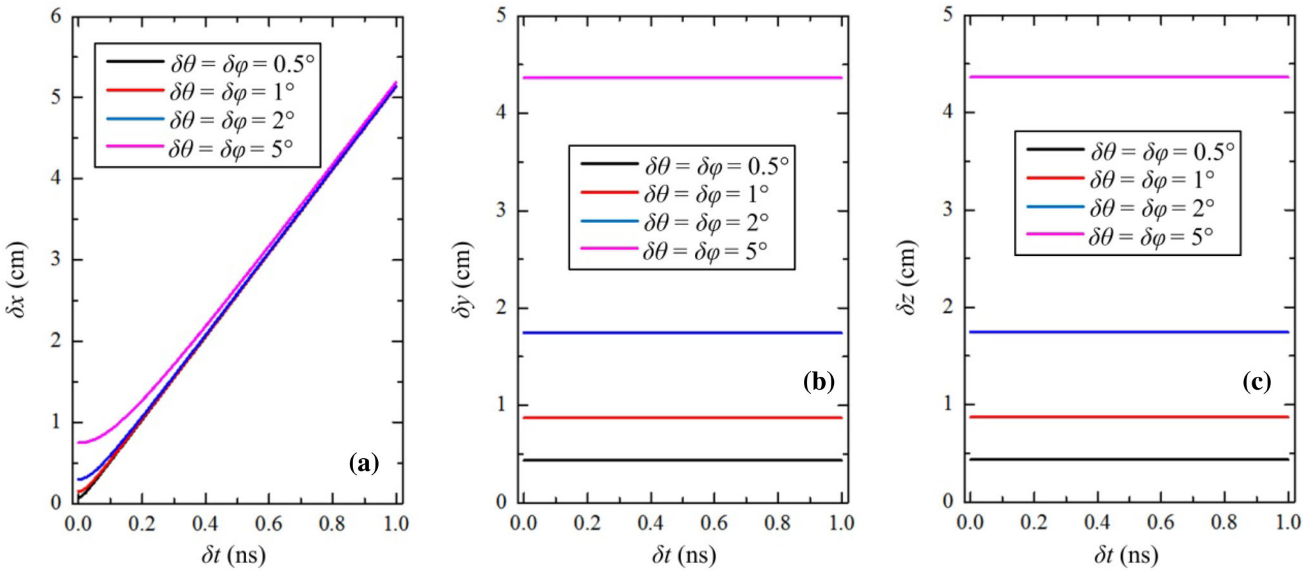

Fig. 5 (Color online) Effect of time resolution and neutron emission angle resolution on the spatial resolution at the origin

5 Monte Carlo simulation of the spatial resolution

To verify the suitability of mathematical analysis and the evaluation of the effects of the spatial resolution of the API-TOF discussed above, a numerical Monte Carlo simulation program, based on the JMCT software [19, 20], was developed to study the API-TOF. The Monte Carlo simulation can reconstruct the spatial distribution of the nuclei of the inspected objects, and it can further calculate the spatial resolution of the API-TOF. By comparing the spatial resolutions calculated using the Monte Carlo simulation and those calculated using the mathematical analysis, the validity of the theoretical analysis discussed in the previous sections can be verified.

The JMCT software is a Monte Carlo simulation software developed by the Beijing Institute of Applied Physics and Computational Mathematics jointly with the Software Center for High Performance Numerical Simulation, China Academy of Engineering Physics. It can accurately simulate neutron, photon, and neutron–photon coupling transports, capable of 3D visual modeling, and high-speed parallel computation [19, 20]. The program developed to study the API-TOF, based on the JMCT software, can simulate the inelastic scatterings and nuclear reactions of neutrons with the nucleus of the inspected object, the production and transport of the characteristic γ-ray, it can reconstruct the spatial position of the nucleus reacting with the neutron, based on the neutron emission direction and the total flight time of the recorded neutrons and γ-ray, and it can further calculate the spatial distribution of the nuclei of the inspected object. Then, by combining the reconstructed spatial distribution of the nuclei of the inspected object with its geometry, the spatial resolution of the API-TOF can be calculated. At the same time, the program can sample the neutron emission direction and the total flight time of the neutron and γ-ray according to the preset time resolution and neutron emission angle resolution of the API-TOF and simulate the effect of the time resolution and the neutron emission angle resolution on the spatial resolution of the API-TOF.

In the simulation, the inspected object was a water cube of 1 cm × 1 cm × 1 cm with the center located at the origin, the angle between the neutron source and the γ-ray detector (∅65 mm × 60 mm) relative to the center of the water cube was 90°, and a typical API-TOF detection device was assumed. The distance between the neutron source and the center of the water cube was 50 cm, which was equal to the distance between the γ-ray detector and the water cube. The energy of the neutrons from the neutron source (point source) was 14.1-MeV, with an isotropic neutron emission direction. As a 6.13-MeV characteristic γ-ray is produced after the inelastic scattering of the 14.1-MeV neutron with ^{16}O in the water cube, the spatial distribution of ^{16}O can be reconstructed based on the emission direction of the 14.1-MeV neutron and the total flight time of the recorded 14.1-MeV neutron and 6.13-MeV γ-ray. Figure 6 shows the reconstructed spatial distribution of ^{16}O on the *y*–*z* plane for three different time resolutions and neutron emission angle resolutions based on the Monte Carlo simulation. It can be seen that with the increase in the time resolution and neutron emission angle resolution, the deviation between the reconstructed spatial distribution and the actual spatial distribution of the ^{16}O increases.

As the volume of the water cube in the simulation is significantly smaller than the distance between the neutron source and the γ-ray detector, the spatial resolutions of the

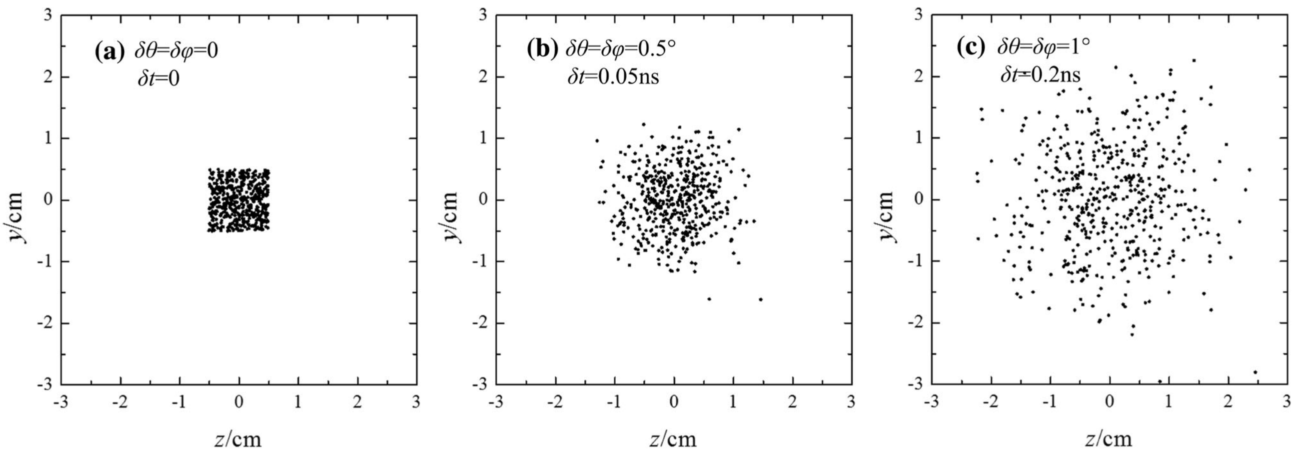

Fig. 6 Reconstructed spatial distributions of ^{16}O for three different time resolutions and neutron emission angle resolutions

Table 1 Spatial resolutions at the origin calculated based on mathematical analysis and Monte Carlo simulation

$\delta\theta$ (°)	$\delta\varphi$ (°)	δt (ns)	Mathematical analysis results			Monte Carlo simulation results		
			δx (cm)	δy (cm)	δz (cm)	δx (cm)	δy (cm)	δz (cm)
0.5	0.5	0.05	0.27	0.44	0.44	0.27	0.43	0.44
1	1	0.1	0.54	0.87	0.87	0.53	0.86	0.87
1	1	0.2	1.04	0.87	0.87	1.03	0.86	0.87
1	1	1	5.14	0.87	0.87	5.11	0.86	0.88
3	3	1	5.16	2.62	2.62	5.13	2.60	2.63
5	5	1	5.19	4.36	4.36	5.18	4.33	4.39

API-TOF detection device in the area where the water cube is located can be regarded as the same approximately. Based on the reconstructed spatial distribution of ^{16}O, the spatial resolution of the API-TOF detection device at the origin can be calculated as

$$\begin{cases} \delta x = \sqrt{\frac{1}{N}\sum_{i=1}^{N} x_i^2 - d_x^2} \\ \delta y = \sqrt{\frac{1}{N}\sum_{i=1}^{N} y_i^2 - d_y^2}, \\ \delta z = \sqrt{\frac{1}{N}\sum_{i=1}^{N} z_i^2 - d_z^2} \end{cases} \tag{14}$$

where N is the number of ^{16}O atoms in the reconstruction image, x_i, y_i, and z_i are the reconstructed spatial coordinates of ^{16}O, and the standard deviations of the reconstructed spatial coordinates of ^{16}O due to the size of the water cube are d_x, d_y, and d_z, respectively. They can be calculated as

$$\begin{cases} d_x = \int_{-\frac{1}{2}}^{\frac{1}{2}} f_1(x)\cdot x^2\cdot \mathrm{d}x \\ d_y = \int_{-\frac{1}{2}}^{\frac{1}{2}} f_2(y)\cdot y^2\cdot \mathrm{d}y, \\ d_z = \int_{-\frac{1}{2}}^{\frac{1}{2}} f_3(z)\cdot z^2\cdot \mathrm{d}z \end{cases} \tag{15}$$

where $f_1(x)$, $f_2(y)$, and $f_3(z)$ are the spatial distribution functions of ^{16}O in the x-, y-, and z-directions in the water cube, respectively, and they are all uniform distribution functions on the interval $\left[-\frac{1}{2}\mathrm{cm}, \frac{1}{2}\mathrm{cm}\right]$.

The calculated values of d_x, d_y, and d_z are all $\frac{1}{2\sqrt{3}}$ cm, and the calculated spatial resolutions of the API-TOF detection device at the origin for different time resolutions and neutron emission angle resolutions are shown in Table 1, which also summarizes the results calculated based on the mathematical analysis. The comparison of the results shows that the spatial resolutions calculated based on the Monte Carlo numerical simulation are in good agreement with those calculated based on the mathematical analysis. Therefore, the mathematical analysis and the evaluation of the effects of the spatial resolution of the API-TOF are verified.

6 Conclusion

In this paper, a study on the spatial resolution of the API-TOF and its effects is presented. The presented results can provide guidance and assist the design of API-TOF detection devices. First, a mathematical analysis of the imaging principles and spatial resolution of the API-TOF was carried out, providing a powerful mathematical tool for the deep understanding of the spatial resolution of API-TOF. Then, the relationship between the device layout and the spatial resolution of the API-TOF detection device was studied, and the concept of a typical API-TOF detection device with an optimized structure was proposed. Next, the effects of the time resolution and the neutron emission angle resolution on the spatial resolution were studied; the results show that by improving the time resolution and the neutron emission angle resolution of the typical API-TOF detection device to appropriate levels, spatial resolutions better than 1 cm can be achieved. Finally, a Monte Carlo numerical simulation program was developed to study the API-TOF. The spatial resolutions calculated based on the Monte Carlo numerical simulation are in good agreement with those calculated based on the mathematical analysis. Therefore, the mathematical analysis and the evaluation of the effects of the spatial resolution of the API-TOF in this study are verified.

References

1. A. Beyerle, J.P. Hurley, L. Tunnell, Design of an associated particle imaging system. Nucl. Instrum. Methods A **299**, 458–462 (1990). https://doi.org/10.1016/0168-9002(90)90825-Q
2. A. Beyerle, R. Durkee, G. Headley et al., Associated particle imaging, in *IEEE NSS-MIC Conference Records*, p. 1298–1304 (1991). https://doi.org/10.1109/nssmic.1991.259135
3. L.E. Ussery, C.L. Hollas, Design and development of the associated-particle three-dimensional imaging technique. The United States: Los Alamos National Laboratory (1994). https://doi.org/10.2172/10183216
4. D.L. Chichester, M. Lemchak, J.D. Simpson, The API 120: a portable neutron generator for the associated particle technique. Nucl. Instrum. Methods B **241**, 753–758 (2005). https://doi.org/10.1016/j.nimb.2005.07.128
5. J.W. Cates, J.P. Hayward, X. Zhang et al., Timing resolution study of an associated particle detector for fast neutron imaging. IEEE Trans. Nucl. Sci. **59**, 1750–1756 (2012). https://doi.org/10.1109/TNS.2012.2201751
6. Q. Ji, B. Ludewigt, J. Wallig et al., Development of a time-tagged neutron source for SNM detection. Phys. Proc. **66**, 105–110 (2015). https://doi.org/10.1016/j.phpro.2015.05.015
7. M.D. Karetnikov, A.I. Klimov, K.N. Kozlov et al., Angular correlations in detection of α–γ coincidences in the nanosecond tagged neutron technology. Nucl. Exp. Tech. **52**, 497–501 (2009). https://doi.org/10.1134/S0020441209040058
8. Kh.E. Bagdasaryan, V.F. Batyaev, S.G. Belichenko et al., Parameters of explosives detection through tagged neutron method. Nucl. Instrum. Methods A **784**, 412–416 (2015). https://doi.org/10.1016/j.nima.2014.11.111
9. M.D. Karetnikov, S.A. Korotkov, T.O. Khasaev, Multidetector system for nanosecond tagged neutron technology based on hardware selection of events. Phys. Part. Nucl. Lett. **13**, 535–540 (2016). https://doi.org/10.1134/S1547477116050277
10. S. Pesente, G. Nebbia, M. Lunardon et al., Tagged neutron inspection system (TNIS) based on portable sealed generators. Nucl. Instrum. Methods B **241**, 743–747 (2005). https://doi.org/10.1016/j.nimb.2005.07.127
11. G. Perret, B. Perot, J.L. Artaud et al., EURITRACK tagged neutron inspection system design. J. Phys: Conf. Ser. **41**, 375–383 (2006). https://doi.org/10.1088/1742-6596/41/1/041
12. B. Perot, G. Perret, A. Mariani et al., The EURITRACK project: development of a tagged neutron inspection system for cargo containers. Proc. SPIE **6213**, 621305 (2006). https://doi.org/10.1117/12.665380
13. B. Perot, C. Carasco, S. Bernard et al., Development of the EURITRACK tagged neutron inspection system. Nucl. Instrum. Methods B **261**, 295–298 (2007). https://doi.org/10.1016/j.nimb.2007.03.073
14. G. Viesti, D. Fabris, M. Lunardon et al., The field use of the EURITRACK tagged neutron inspection system. AIP Conf. Proc. **1336**, 693–695 (2011). https://doi.org/10.1063/1.3586191
15. W. El Kanawati, B. Perot, C. Carasco et al., Conversion factors from counts to chemical ratios for the EURITRACK tagged neutron inspection system. Nucl. Instrum. Methods A **654**, 621–629 (2011). https://doi.org/10.1016/j.nima.2011.05.076
16. K. Xiao, D. Jin, W. Xiang et al., The design of neutron generator with concomitant particle. Nucl. Tech. **34**, 27–30 (2011). **(in Chinese)**
17. X.H. Wang, P. Zheng, L. An et al., Development of a hidden explosives security check instrument based on associated particles technique. High Power Laser Part. Beams **26**, 059002-1–059002-5 (2014). **(in Chinese)**
18. M. Bouhrara, R.G. Spencer, Fisher information and Cramér–Rao lower bound for experimental design in parallel imaging. Magn. Reson. Med. **79**, 3249–3255 (2018). https://doi.org/10.1002/mrm.26984
19. G. Li, B.Y. Zhang, L. Deng et al., Development of Monte Carlo particle transport code JMCT. High Power Laser Part. Beams **25**, 158–162 (2013). **(in Chinese)**
20. L. Deng, G. Li, B.Y. Zhang et al., Simulation of full-core pin-by-pin model by JMCT Monte Carlo neutron–photon transport code. At. Energy Sci. Technol. **48**(6), 1061–1066 (2014). **(in Chinese)**